# Near-Field Optical Properties of Ag x Au1–x Nanoparticle Chains Embedded in a Dielectric Matrix

Alexandre Fafin, Senda Yazidi, Sophie Camelio, David Babonneau

**Noname manuscript No.**
(will be inserted by the editor)

# Near-field optical properties of $Ag_xAu_{1-x}$ nanoparticle chains embedded in a dielectric matrix

**Alexandre Fafin · Senda Yazidi · Sophie Camelio · David Babonneau**

December 21, 2015

**Abstract** We study by the finite-difference time-domain method the near-field optical properties of isolated or coupled $Ag_xAu_{1-x}$ alloy nanoparticles shallowly buried inside dielectric matrices. The optical index of alloys are obtained experimentally using spectroscopic ellipsometry measurements from multilayered thin films fabricated by ion-beam sputtering. Then, we numerically investigate the influence of the nanoparticle composition, interparticle gap and capping-layer thickness on the amplitude and spatial extent of the electric field in the vicinity of ellipsoidal nanoparticles. Our calculations provide evidence that pure metal nanoparticles (Ag or Au) exhibit a greater field enhancement associated with a larger out-of-plane extent compared to alloy nanoparticles, an effect that is even more pronounced when the optical index of surrounding matrix is increased. Moreover, we show that the optimal gap between nanoparticles to maximize the amplitude of the electric field at the capping layer/air interface results from a delicate balance, which strongly depends on the thickness of the dielectric capping layer.

**Keywords** Localized surface plasmon resonance (LSPR) · Ag-Au alloy nanoparticles · Finite-difference time-domain method (FDTD) · Near-field enhancement · SERS

**PACS** 78.67.-n · 78.20.-e · 78.20.Bh · 78.20.Ci

A. Fafin · S. Yazidi · S. Camelio · D. Babonneau
Institut Pprime, Département Physique et Mécanique des Matériaux, UPR 3346 CNRS, Université de Poitiers, SP2MI, 11 Bvd M. et P. Curie, BP 30179, F-86962 Futuroscope Chasseneuil Cedex, France
E-mail: alexandre.fafin@univ-poitiers.fr

## 1 Introduction

The interaction of a noble metal nanoparticle with incident light of specific wavelength induces a localized surface plasmon resonance (LSPR), i.e. a collective oscillation of the conduction electrons at the surface of the nanoparticle. The wavelength of LSPR depends on the morphology (shape and size) and composition of the nanoparticle as well as the refractive index of the host medium [1,2]. One of the LSPR properties is to enhance the electric field in the immediate vicinity of the nanoparticle. This field enhancement can be increased by coupling two nanoparticles, i.e. by reducing the interparticle gap to less than about one or two nanoparticle diameters. Thus, nanoparticles arranged as sub-wavelength arrays of chains are good candidates to increase the electric field intensity by several orders of magnitude in localized regions, which are called hot spots. There are multiple applications of such arrays of nanoparticles like light-harvesting devices [3], but also as active surfaces for surface-enhanced fluorescence [4, 5] and surface-enhanced Raman scattering (SERS) [6,7, 8]. Therefore, the fabrication of substrates with a high density of hot spots, i.e. with controlled narrow gaps between metal nanoparticles, is a challenge of current research. In recent works [9,10,11,12,13,14,15,16,17, 18,19,20,21], it has been proposed to fabricate such substrates by engineering a dielectric surface by ion-beam sputtering or thermal annealing followed by the growth of metallic nanoparticles (Ag, Au, Al) by physical vapor deposition at glancing-incidence angle. Using this method, periodic chains of elongated nanoparticles with dimensions and gaps below the resolution of lithographic techniques can be formed. Moreover, these nanoparticle chains can be coated with a dielectric capping layer, which provides stability against ageing ef-

fects and temperature, but also enables surface cleaning without modification of their optical properties. However, the capping layer must be as thin as possible because the electric field is evanescent. In Refs. [9,10, 11,12,13,14,15,16], Ag nanoparticles have been investigated because Ag is known to product an important field enhancement. However, this metal has a high mobility and a poor chemical stability, which may force to use a capping layer too thick to obtain an acceptable field enhancement at the capping layer/air interface. Compared to Ag, Au is known to present a lower field enhancement, nevertheless it has a lower atomic mobility and a better chemical stability against corrosive environments. It would therefore be possible to use a thinner capping layer, which could allow to preserve sufficient electric field intensity at the surface of the capping layer. Recently, it has been proposed to use $Ag_xAu_{1-x}$ alloy nanoparticles to combine the respective advantages of high field enhancement of Ag and chemical inertness of Au [22]. Indeed, it has been shown that $Ag_xAu_{1-x}$ alloy nanoparticles increase their oxidation resistance with the Au fraction $(1-x)$ [23]. Moreover, alloy nanoparticles can reduce the Ag ion release upon immersion in water [24]. While the far-field optical properties of $Ag_xAu_{1-x}$ nanoparticles prepared by various chemical [25,26,27] and physical [28,29,30, 31,32,33] methods are widely documented, the near-field properties have not been studied extensively until now [34].

The objective of this paper is to compare numerically, by the finite-difference time-domain (FDTD) method, the near-field optical properties of isolated and coupled $Ag_xAu_{1-x}$ nanoparticles ($0 \leq x \leq 1$) sandwiched between dielectric layers. Particular attention is paid to the influence of the nanoparticle composition, interparticle gap and capping-layer thickness on the amplitude and spatial extent of the hot spots. The paper is organized as follows: in section 2, we present the production process of $Ag_xAu_{1-x}$ alloy thin films and the determination of their complex refractive index by spectroscopic ellipsometry. Then, in section 3, we study the optical properties of isolated metallic nanoparticles embedded inside dielectric matrices ($SiO_2$, $Al_2O_3$, $Si_3N_4$). Finally, in section 4, we investigate the case of nanoparticle chains, and more particularly the role of coupling effects on the amplitude of the electric field at the capping layer/air interface.

## 2 Refractive index of $Ag_xAu_{1-x}$ alloy thin films

In order to determine the optical properties of $Ag_xAu_{1-x}$ nanoparticles by the FDTD method, the complex refractive index of bulk alloys has to be known. Actually, a composition-weighted average of Ag and Au permittivities $\varepsilon_{\text{alloy}} = x\varepsilon_{\text{Ag}} + (1-x)\,\varepsilon_{\text{Au}}$, where $x$ is the Ag volume fraction, does not reproduce faithfully the permittivity $\varepsilon_{\text{alloy}}$ of a $Ag_xAu_{1-x}$ alloy (especially in the near-infrared region), because the band structure of $Ag_xAu_{1-x}$ alloys is different from pure Ag or Au metals [35,36,37]. Thus, $Ag_xAu_{1-x}$ alloys cannot be pictured as the gathering of small homogeneous Ag and Au domains. However, there are few experimental studies which address the determination of the optical index of $Ag_xAu_{1-x}$ alloys [38,39,34]. In a recent study, Peña-Rodríguez *et al.* [38] obtained the refractive index of $Ag_xAu_{1-x}$ alloy thin films fabricated by electron beam co-evaporation. Other studies reported refractive index measurements of $Ag_xAu_{1-x}$ alloys from films produced by co-evaporation [39] or by alternate evaporation with individual layer thicknesses below 1 nm [34]. These works highlight the fact that the refractive index of metal alloys may be different according to the preparation conditions [40,41]. In order to compare our FDTD calculations with experimental results on $Ag_xAu_{1-x}$ nanoparticles [42], we therefore prepared our own samples and we determined experimentally their optical properties using spectroscopic ellipsometry measurements.

**Table 1** Thickness of the individual metal layers and number of bilayers $m$ of $(Au/Ag)_m$ multilayers grown on sapphire substrates.

| Composition | Thickness (nm) | | $m$ |
|---|---|---|---|
| | Au | Ag | |
| Au | 103.5 | - | 1 |
| $Ag_{0.26}Au_{0.74}$ | 2.7 | 0.9 | 25 |
| $Ag_{0.41}Au_{0.59}$ | 2.7 | 1.9 | 20 |
| $Ag_{0.62}Au_{0.38}$ | 1.9 | 3.1 | 20 |
| $Ag_{0.75}Au_{0.25}$ | 1.0 | 3.1 | 25 |
| Ag | - | 98.7 | 1 |

$(Au/Ag)_m$ multilayers with various compositions were first grown on sapphire substrates by alternate ion-beam sputtering deposition in a Nordiko 3000 chamber. Deposition rates of Ag and Au were $v_{\text{Ag}} = 0.235$ nm/s and $v_{\text{Au}} = 0.207$ nm/s, respectively. The number $m$ of Au/Ag bilayers was adjusted to obtain a total thickness of about 100 nm. In order to facilitate alloy formation during annealing at 400 °C for 1h under vacuum ($\simeq 2.10^{-7}$ mbar), the thickness of individual metal layers was less than 3 nm (Table 1). The structure of the as-deposited multilayers was investigated by X-ray reflectivity (XRR). An example of specular XRR curve is presented in Fig. 1 for the as-deposited $Ag_{0.62}Au_{0.38}$ multilayer. The Bragg peak located at $\theta \simeq 1.03°$ is characteristic of the periodic structure of the multilayer. Af-

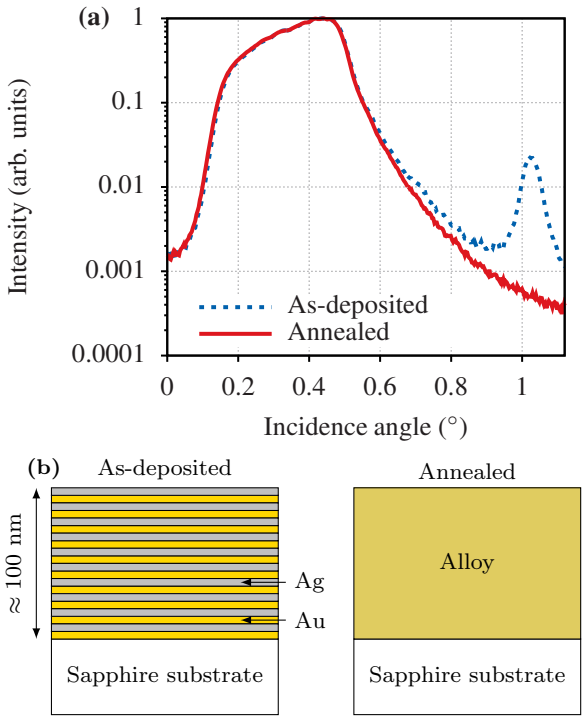


**Fig. 1** (a) Specular XRR curves measured for the $Ag_{0.62}Au_{0.38}$ multilayer as-deposited and after annealing at 400 °C for 1h under vacuum. (b) Schematic drawing of the corresponding film structures.

ter annealing, we can notice that the Bragg peak disappeared, thus proving that the multilayer structure vanished and suggesting the formation of a $Ag_{0.62}Au_{0.38}$ alloy thin film. It should be noted that this behaviour was similar for all $(Au/Ag)_m$ multilayers.

Refractive index of the annealed samples were determined by spectroscopic ellipsometry measurements in the ultraviolet-visible range (210 − 800 nm) with a SOPRA GESP5 ellipsometer (Fig. 2). Because the total thickness of these pure metal or alloyed films is around 100 nm, we considered that the incident field is null at the sapphire substrate interface and the measured ellipsometric data were transformed into optical index assuming bulk materials. For pure Ag and Au, interband transitions start for a wavelength greater than about 340 nm and 550 nm, respectively. The region of the onset for interband transitions varies smoothly as a function of the film composition. However, in the near-infrared region, the real part $n$ of the refractive index for the alloys are higher than those of both pure metals, as previously reported in Ref. [38].

We analyzed the refractive index of the $Ag_xAu_{1-x}$ alloys by a Drude model [2] where the permittivity $\varepsilon$ can be written as

$$\varepsilon(\omega) = \varepsilon_\infty - \frac{\omega_p^2}{\omega^2 + i\omega\Gamma}, \quad (1)$$

where $\varepsilon_\infty$ is the high-frequency contribution of the bound electrons, $\omega_p$ is the bulk plasma frequency, and $\Gamma$ is the damping constant due to scattering events at defects and grain boundaries. According to Ref. [38], fits of the refractive index were performed in the energy range below interband transitions, i.e. $\hbar\omega \simeq 3.1$ eV (400 nm) for Ag and $\hbar\omega \simeq 2.1$ eV (600 nm) for Au. For $Ag_xAu_{1-x}$ alloys, we assumed that the energy of interband transitions varies linearly as a function of the composition [28].

Results of fits for $\omega_p$ and $\Gamma$ for all $Ag_xAu_{1-x}$ alloys are shown in Fig. 3. For comparison $\omega_p$ and $\Gamma$ values for pure metal films (as-deposited and annealed) and those determined from data of Johnson and Christy [43] are also represented. For pure metals, annealing causes a decrease of both the plasma frequency $\omega_p$ and damping constant $\Gamma$. This is an indication that, in particular with regard to the value of $\Gamma$, annealed films are more ordered and contains fewer defects that contribute to dampen the motion of the conduction electrons [44]. Moreover, we observe that both $\omega_p$ and $\Gamma$ values do not vary linearly with Ag fraction. By an analytical model, Rioux *et al.* [45] found that the plasma frequency $\omega_p$ follows a parabolic law as a function of the alloy composition, which is not inconsistent with our values. Regarding the damping constant, $\Gamma$ is minimum for pure Ag and Au metals and increases for $Ag_xAu_{1-x}$ alloys showing that alloys can be considered as more disordered materials than pure metals at the atomic scale. As a result, the average time interval $\tau \propto 1/\Gamma$ between scattering events is lower for alloys than for pure metals [2]. In Refs. [38,45,46,47], $\Gamma$ was found to follow a parabolic law as a function of the alloy composition, while in the volume fraction range 0.26-0.75 screened in this study, $\Gamma$ is quasi-constant. Finally, the contribution of the bound electrons $\varepsilon_\infty$ (not shown here) varies linearly between 9.6 for Au and 4.1 for Ag. All these values are consistent with those found by Peña-Rodríguez *et al.* on co-evaporated $Ag_xAu_{1-x}$ alloys [38].

## 3 Near-field optical properties of isolated nanoparticles

In this section, we study the near and far-field properties of isolated nanoparticles in order to compare the optical response between alloy and pure metal nanoparticles embedded in a dielectric matrix. We used a commercial-grade simulator based on the FDTD method [48] to perform the calculations with the configuration presented in Fig. 4. The nanoparticles were assumed to be ellipsoidal with the dimensions $a = 5$ nm, $b = 4$ nm and $c = 2.5$ nm, which correspond to average experimental

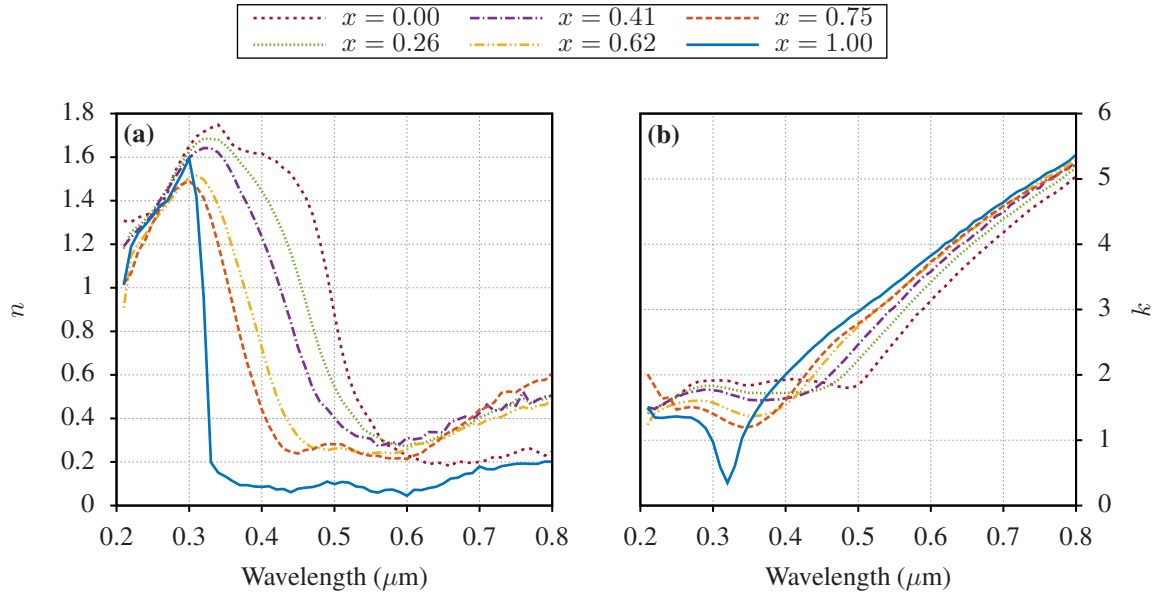


**Fig. 2** (a) Real part $n$ and (b) imaginary part $k$ of the refractive index $\tilde{n}$ of annealed $Ag_xAu_{1-x}$ multilayers.

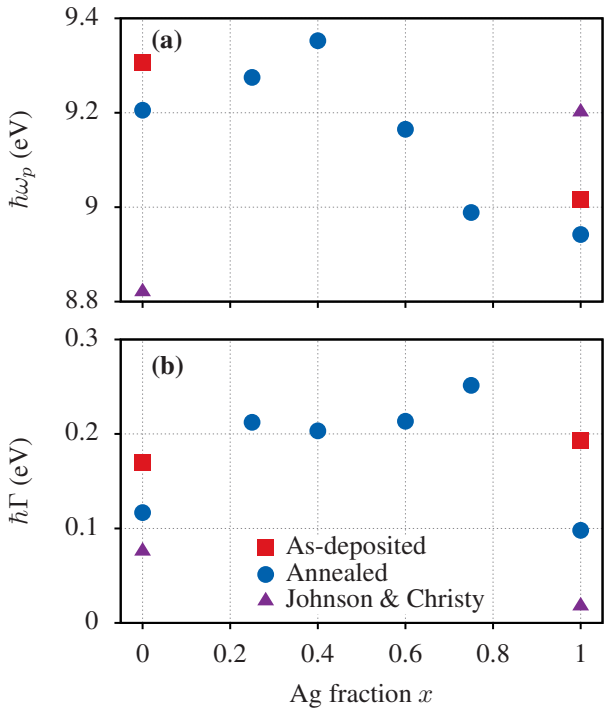


**Fig. 3** (a) Plasma frequency $\omega_p$ and (b) damping constant $\Gamma$ as a function of the Ag fraction $x$ in various $Ag_xAu_{1-x}$ alloys.

dimensions determined in a previous work [16]. Refractive indices of $Ag_xAu_{1-x}$ alloys determined in section 2 were described by a Drude-Lorentz model. For all compositions, we ignored non-local effects, which are known to increase the damping constant $\Gamma$ contribution to the

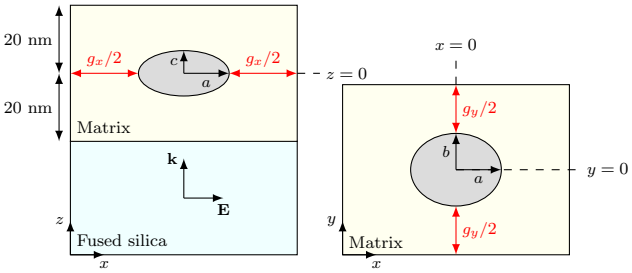


**Fig. 4** Sketch of the configuration used to perform FDTD calculations for $Ag_xAu_{1-x}$ nanoparticles surrounded by a dielectric matrix deposited on a fused silica substrate in $(xz)$ plane (on the left) and in $(xy)$ plane (on the right). Dimensions of the ellipsoidal nanoparticle are $a = 5$ nm, $b = 4$ nm and $c = 2.5$ nm. Direction of propagation and polarization of the incident electric field are also represented. The origin of the coordinates is taken at the center of the particle.

permittivity [49]. To ensure a good stability and accurate results of calculations, we used a non-uniform mesh with a space step equal to 0.1 nm to model the nanoparticles and their vicinity. We used periodic boundary conditions in $x$ and $y$ directions with a large gap in order to ensure that particles were not coupled (the gaps between two nanoparticles were $g_x = 50$ nm and $g_y = 52$ nm in $x$ and $y$ directions, respectively). The choice of periodic boundary conditions with respect to perfectly matched layer (PML) [50] absorbing boundaries is motivated by the memory space reduction. In $z$ direction, we used PML boundary conditions. We have tested three dielectric matrices (40 nm total thickness) whose refractive indices were determined from spectroscopic ellipsometry measurements of amorphous

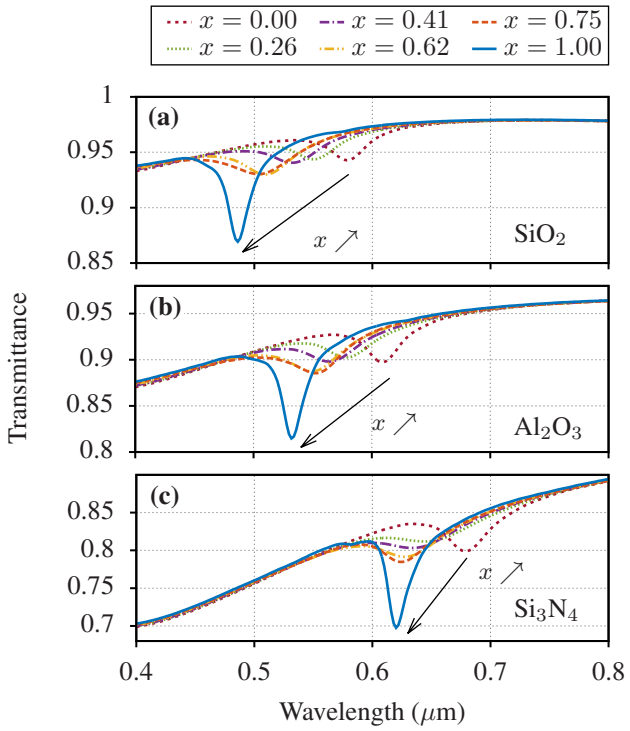


**Fig. 5** Transmission spectra calculated at normal incidence with a longitudinal excitation for isolated ellipsoidal $Ag_xAu_{1-x}$ nanoparticles embedded in (a) $SiO_2$ matrix, (b) $Al_2O_3$ matrix, and (c) $Si_3N_4$ matrix.

$SiO_2$, $Al_2O_3$ and $Si_3N_4$ films (sorted here by increasing refractive index: $n_{SiO_2} = 1.46$, $n_{Al_2O_3} = 1.66$ and $n_{Si_3N_4} = 2.05$ at $\lambda = 600$ nm). Here, the thickness of the dielectric film above the particles was equal to 17.5 nm (dielectric/air interface located at $z = 20$ nm). The thickness of the fused silica substrate was set to 100 nm, which is a compromise between an infinite substrate and acceptable memory requirement. Still to limit the memory requirement, the refractive index of the substrate was assumed to be independent of the wavelength and equal to 1.45. The nanoparticles were excited by an incident plane wave located in the substrate region, propagating along the $z$ axis, and polarized along the $x$ axis.

The transmission spectra, recorded far from the nanoparticle at $z = 40$ nm, for the three host matrices are presented in Fig. 5. In all cases the spectral position $\lambda_r$ of the LSPR is blue-shifted when increasing the Ag fraction $x$, which is the usual result [38,45,39]. The baseline differences come from the refractive index of the matrix. For a high refractive index matrix, like $Si_3N_4$, the blue-shift is however less pronounced than for a low refractive index as $SiO_2$. The variation of the LSPR position is not linear with the Ag fraction $x$ contrary to what is reported in Refs. [46,35,51,22]. As mentioned by Verbruggen *et al.* [52], for a spherical nanoparticle in water, a third-order dependence is more adapted.

Typical $|E(x,z)|/|E_0|$ maps calculated at the LSPR wavelength for pure Ag and Au nanoparticles embedded in $Al_2O_3$ are displayed in Fig. 6. It can be observed that the maximum of field enhancement $|E|_{max}/|E_0|$ is located at the tip of the nanoparticles ($x = \pm a$ and $y = z = 0$). Furthermore, the field enhancement is greater for Ag than for Au, as expected. In Fig. 6, $|E|_{max}/|E_0|$ values obtained at the LSPR wavelength are plotted versus the Ag fraction $x$. First of all, we can notice that the field enhancement is higher for pure metals than for alloys, with a minimum for $x = 0.5$, which is mainly due to the high value of the damping constant $\Gamma$. Therefore, although the use of alloy nanoparticles can be a good solution for varying accurately the LSPR wavelength, this reduces dramatically the field enhancement. We can also notice that the field enhancement of pure metal nanoparticles is higher inside a high index dielectric matrix. For example, comparing $SiO_2$ and $Si_3N_4$ for a pure Ag nanoparticle, the field enhancement is increased by about 33%. Nevertheless, for alloys, the nature of the matrix has less influence on the field enhancement. Thus, for tuning the LSPR wavelength without strongly reducing the field enhancement, it would be preferable to change the dielectric matrix surrounding pure metal nanoparticles instead of using alloy nanoparticles. From $|E(x,z)|/|E_0|$ maps it is possible to extract the decay length of the electric field in $x$ and $z$ directions by a fit of the electric field decay from the tip of the nanoparticle where the field is maximum by assuming an exponential law (Eq. 2):

$$\frac{|E(i)|}{|E_0|} = \frac{|E|_{max}}{|E_0|} \exp(-\frac{i}{L_i}) + 1 \qquad \text{where } i = x, z \qquad (2)$$

where $L_i$ corresponds to the distance at which the electric field is reduced to 37% of its maximal value $|E|_{max}/|E_0|$. The evolution of the decay lengths along $x$ direction, $L_x$, and along $z$ direction, $L_z$, are represented in Fig. 7 as a function of the composition of the nanoparticles. It appears that $L_x$ is almost constant and does not depend on the refractive index of the dielectric matrix. The important errors bars underline the fact that the electric field does not really decrease by an exponential low. In fact, if we consider that the nanoparticle behaves as a dipole, the electric field should decay as $1/r^3$, where $r$ is the radial distance [2]. In contrast, $L_z$ is not only more important for pure metal than for alloy nanoparticles, but also the influence of the dielectric matrix on $L_z$ seems to depend on the nanoparticle composition. For pure metals, $L_z$ is greater for a high refractive index matrix, while for alloys it is not obvious to identify any

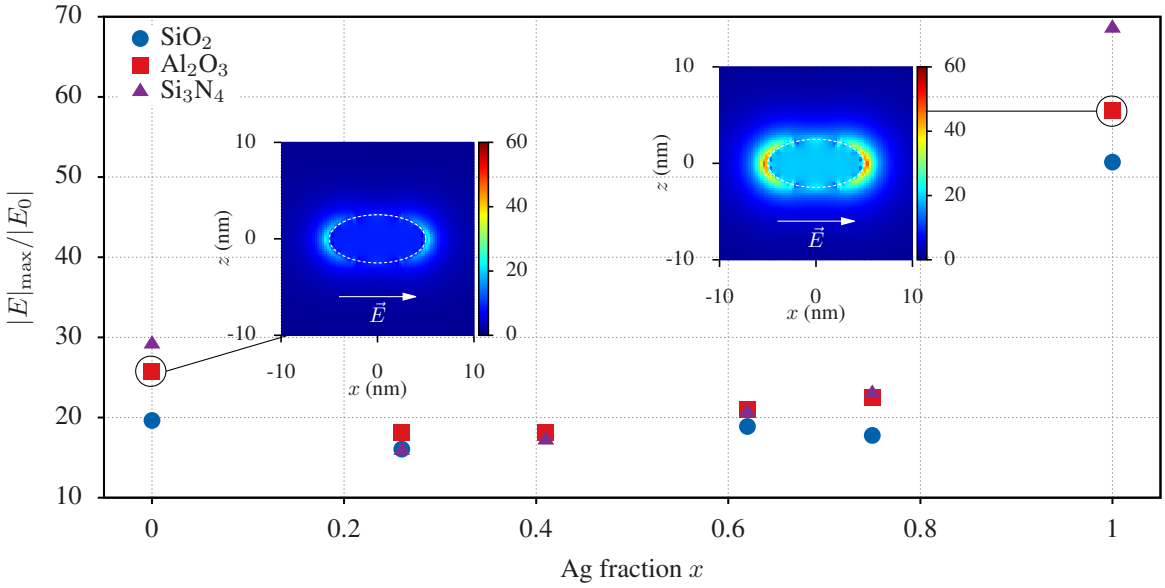


**Fig. 6** Maximum of the field enhancement $|E|_{\max}/|E_0|$ obtained at the LSPR wavelength as a function of the Ag fraction $x$ for isolated nanoparticles embedded in $SiO_2$, $Al_2O_3$ and $Si_3N_4$ matrices. Insets: field enhancement $|E(x,z)|/|E_0|$ maps calculated at the LSPR wavelength for Ag and Au nanoparticles in $Al_2O_3$ matrix. Dotted lines indicate dimensions and position of the nanoparticle.

effect. By comparing $L_x$ and $L_z$, we can notice that the decay length is more important in $z$ direction. This is due to the ellipsoidal shape of the nanoparticles, which induces an anisotropic emission from the tip. In order to have an important field enhancement above a shallowly buried nanoparticle, ellipsoidal nanoparticles of pure metals are thus a relevant choice.

## 4 Near-field optical properties of nanoparticle chains

In order to study the influence of coupling effects on the amplitude and spatial extent of the electric field enhancement, we still applied a large and constant gap in $y$ direction ($g_y = 52$ nm) but a small and variable gap $g_x$ in $x$ direction (Fig. 4). To limit the number of parameters, we only considered the case of nanoparticle chains embedded in $Al_2O_3$. The parameters investigated in this section are the composition of the nanoparticles, the gap $g_x$ and the capping-layer thickness.

As done in section 3 in the case of isolated nanoparticles, transmission spectra were first calculated for various compositions and gaps $g_x$ between nanoparticles. Figure 8(a) shows the evolution of the fractional plasmon shift $\Delta\lambda/\lambda_r$ as a function of $g_x/2a$. Whatever the Ag fractions $x$, when $g_x$ decreases, the LSPR of the nanoparticle chains is red-shifted ($\Delta\lambda > 0$). The plasmon shift can be approximated by an exponential law known as "plasmon ruler equation" [53,54,55]:

$$\frac{\Delta\lambda}{\lambda_r} = A \exp\left(-\frac{g_x/2a}{\tau_0}\right), \tag{3}$$

where $\lambda_r$ is the LSPR wavelength of a single particle, $\Delta\lambda$ is the spectral shift of the LSPR for an array of nanoparticles with respect to the single particle, $\tau_0$ is an exponential decay constant, and $A$ is a pre-exponential fitting factor. $\tau_0$ is a parameter that depends on the size and shape of the nanoparticles, with a typical value ranging between 0.15 and 0.35 [55], and which is often assimilated to $L_x$ [55,53]. Figure 8(b) shows the decay values $\tau_0$ of the best fit for different nanoparticle compositions. We can notice that $\tau_0$ depends on the composition of the nanoparticles, and increases with the Ag fraction. This is a surprising result because, when considering isolated nanoparticles, the decay length along $x$ direction is constant for all compositions (Fig. 7). It is therefore wise not to consider, for an array of nanoparticles, $\tau_0$ as a decay length in units of the particle size [55,53]. Moreover, as we have seen in Section 3, considering a single decay length is an oversimplification for a nanoparticle which is not a sphere. So, to obtain valuable information about the near-field properties, $|E|/|E_0|$ maps were calculated at the LSPR wavelength for various compositions and gaps.

As for isolated nanoparticles, we plot in Fig. 9 the maximum field enhancement $|E|_{\max}/|E_0|$ located at the tip of the nanoparticles in the $(xy)$ plane at $z = 0$.

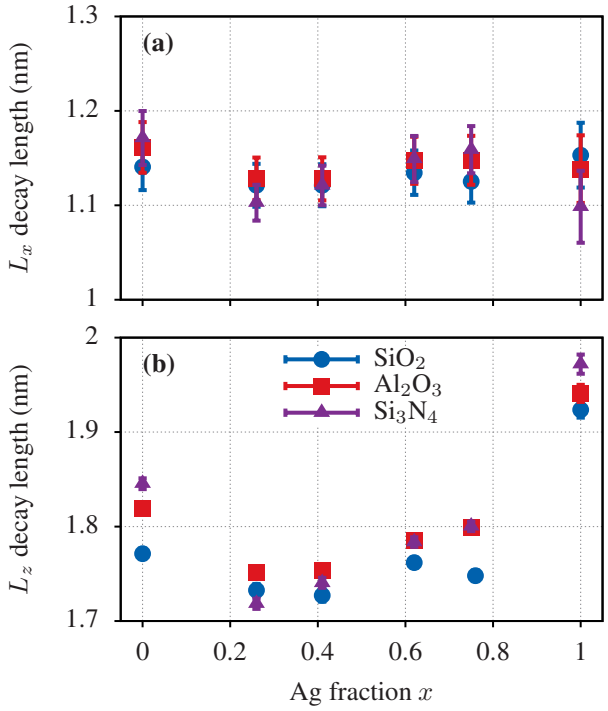


**Fig. 7** Decay length as a function of the Ag fraction along (a) $x$ direction and (b) $z$ direction.

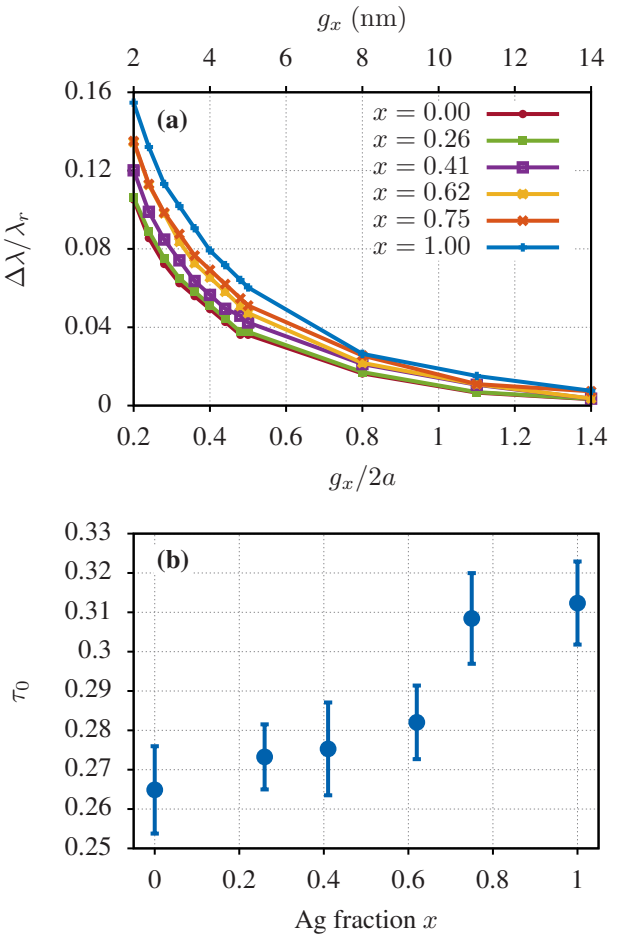


**Fig. 8** (a) Evolution of the fractional plasmon shift $\Delta\lambda/\lambda_r$ as a function of the gap $g_x$ between ellipsoidal $Ag_xAu_{1-x}$ nanoparticles. (b) $\tau_0$ values extracted by the fit of (a) with Eq. 3.

When the interparticle gap decreases, the maximum field enhancement increases, which is a known result [56]. As for isolated nanoparticles, we find that the field enhancement is always more important for pure metals than for alloys. For $g_x/2a$ greater than 0.8, i.e. for a gap greater than 8 nm, the field enhancement tends to that of isolated nanoparticles.

For SERS-type applications with protected nanoparticles, it is necessary to have an important field enhancement at the surface of the capping layer. The decay length along $z$ direction, $L_z$, is therefore particularly interesting. $L_z$ values calculated starting from the tip of the nanoparticles are displayed in Fig. 10. We observe that $L_z$ drops when the gap decreases owing to the field confinement effect. Hence, depending on the thickness of the capping layer, we can anticipate that a smaller gap does not necessarily yield the highest field enhancement at the capping layer/air interface. Figure 11 shows the $g_x$ dependence of the maximum of the field enhancement for different altitudes $z$ from the nanoparticle tip ($x = a$ and $y = 0$). First, we can notice again that the field enhancement is always greater for pure metals than for alloys whatever the distance $z$ from the hot spot. Secondly, we can observe three different regimes:

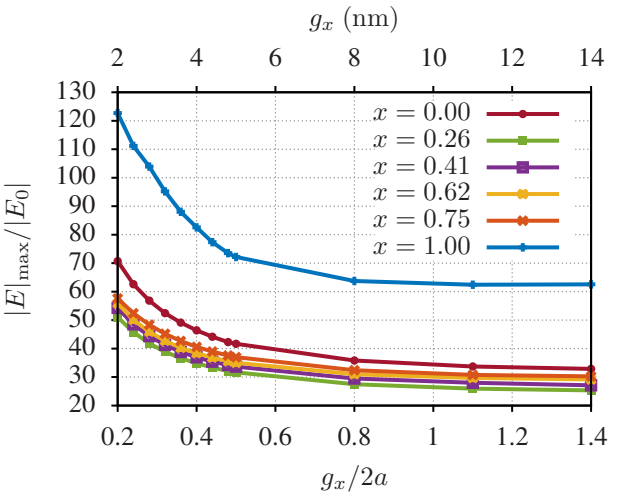


**Fig. 9** Maximum field enhancement $|E|_{max}/|E_0|$ as a function of $g_x$ for an array of ellipsoidal $Ag_xAu_{1-x}$ nanoparticle chains.

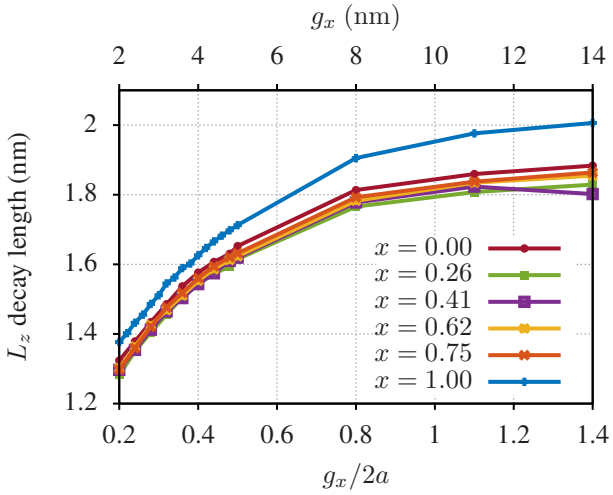


**Fig. 10** Decay length along $z$ direction as a function of $g_x$ for an array of ellipsoidal $Ag_xAu_{1-x}$ nanoparticle chains.

- For $z \leq 3$ nm, the gap $g_x$ should be as small as possible to have the maximum field enhancement.
- For $z \geq 5$ nm, the field enhancement is maximum for a large gap, i.e. for isolated nanoparticles.
- For intermediate $z$ values, the field enhancement is almost constant with $g_x$ and displays a small bump for a gap between 3 and 4 nm, depending on the composition of the nanoparticles. For pure Ag the maximum is reached for 3 nm whereas it is around 4 nm for pure Au and alloys.

To confirm these results obtained for nanoparticles embedded in a dielectric matrix with a capping-layer thickness equal to 17.5 nm (Fig. 4), we performed calculations for Ag and Au nanoparticles by assuming a capping layer/air interface located at $z = 3$ nm and $z = 5$ nm, respectively. Figs. 12 and 13 show field enhancement $|E(x, y)|/|E_0|$ maps above the capping layer/air interface for gaps $g_x = 2$ nm and $g_x = 14$ nm, respectively. For clarity, dotted lines indicates the position and dimension of the nanoparticles below the capping layer at $z = 0$ nm. Compared to Fig. 11, $|E|/|E_0|$ values obtained at $x = 5$ nm and $y = 0$ nm are slightly larger owing to the discontinuity of the optical index at the capping layer/air interface, which tends to increase the field amplitude in the air media. Furthermore, we can note that the maximum field enhancement $|E|_{\max}/|E_0|$ at an altitude $z$ is not located just above the tips ($x = \pm 5$ nm, $y = 0$ nm) of the nanoparticles. Actually, increasing the interparticle gap or the capping-layer thickness, we observe that $|E|_{\max}/E_0$ at the capping layer/air interface moves closer to $x = 0$. For example, when considering Ag nanoparticles with $z = 3$ nm, $|E|_{\max}/|E_0|$ is located at $x = \pm 4.2$ nm for $g_x = 2$ nm [Fig. 12(c)] whereas it is positioned at $x = \pm 3.7$ nm for $g_x = 14$ nm [Fig. 13(c)].

Overall, these calculations confirm firstly that for a given gap $g_x$, the thinner the capping layer, the higher the field enhancement for both metals. Secondly, for the same capping-layer thickness, the field amplification at the capping layer/air interface is always greater for Ag nanoparticles than for Au ones whatever the gap $g_x$. Nevertheless, it is worth noting that the field amplification is greater for Au nanoparticles with a 3 nm-thick capping layer [Figs. 12(a) and 13(a)] than for Ag nanoparticles with a 5 nm-thick capping layer [Figs. 12(d) and 13(d)]. Moreover, comparisons between Figs. 12(b), 12(d) and Figs. 13(b), 13(d) corroborate the previous results drawn from Fig. 11, namely the maximum field enhancement obtained with a 5 nm-thick capping layer is higher for a gap $g_x = 14$ nm than for $g_x = 2$ nm, i.e. for uncoupled nanoparticles. In contrast, with a 3 nm-thick capping layer, it would be preferable to have coupled nanoparticles. Accordingly, for SERS-type applications, both the thickness of the capping layer and the interparticle gap are parameters that must be precisely controlled. For strongly coupled nanoparticles, the thickness of the protective layer must be minimized while allowing the chemical stability and limiting atomic diffusion of the metal. These results are clearly valid for the nanoparticle size considered in this paper. Increasing the size of the nanoparticle allows to increase the field enhancement at the dielectric/air interface for a same thickness of capping layer, but it reduces the areal density of hot spots. Therefore, it appears that a delicate and not intuitive compromise has to be found to reach the best field-enhancement effect.

## 5 Conclusion

In summary, we have investigated the near-field optical properties of isolated or coupled ellipsoidal $Ag_xAu_{1-x}$ nanoparticles embedded inside a dielectric matrix by the FDTD method. We have demonstrated that the field enhancement for pure metal nanoparticles (Ag or Au) is higher than for $Ag_xAu_{1-x}$ alloy nanoparticles. The optical index of the dielectric matrix surrounding the nanoparticles has an influence on the spectral position of the LSPR, but also on the amplitude and spatial extent of the electric field enhancement. Especially for pure metal nanoparticles, a high matrix index results in a greater field enhancement together with a more important decay length is in $z$ direction. Regarding the near-field optical properties for coupled nanoparticles, we have shown that reducing the interparticle gap increases the amplification and the confinement of the

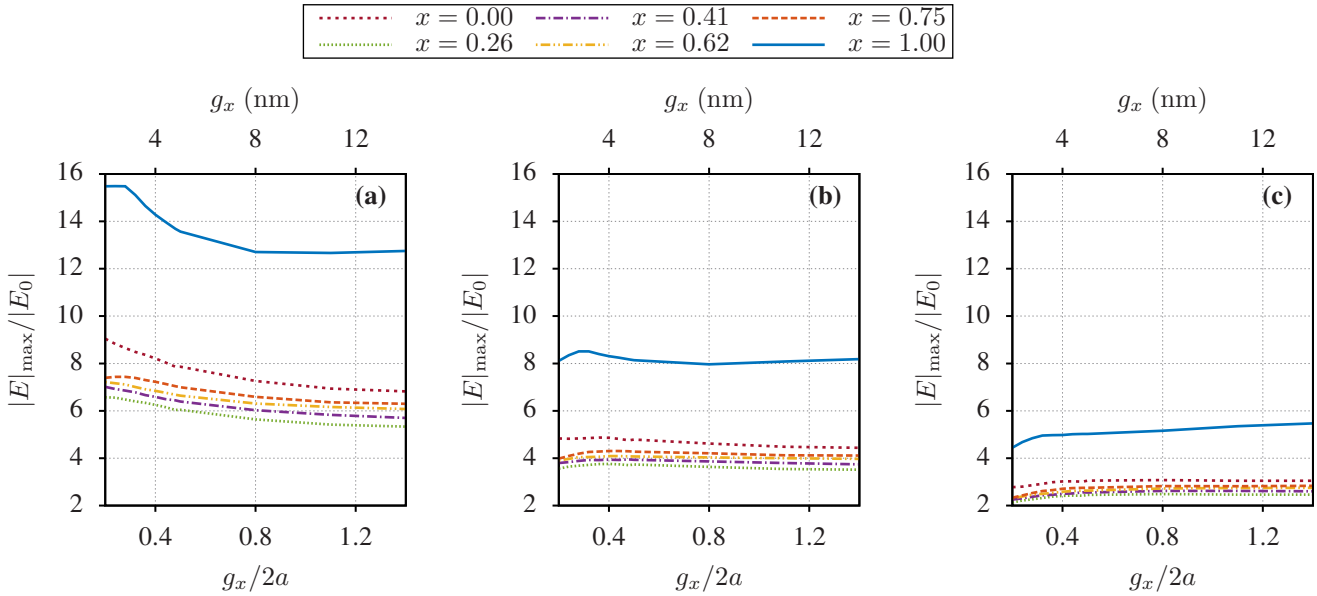


**Fig. 11** Maximum field enhancement $|E|_{\max}/|E_0|$ at a distance (a) $z = 3$ nm, (b) $z = 4$ nm, and (c) $z = 5$ nm from the hop spot as a function of $g_x$ for an array of ellipsoidal $Ag_xAu_{1-x}$ nanoparticle chains capped by a 20 nm-thick $Al_2O_3$ film.

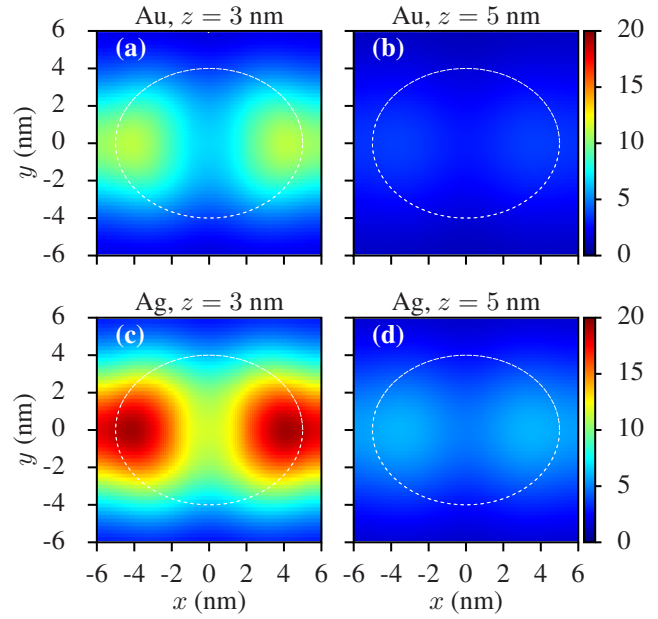


**Fig. 12** Field enhancement $|E(x, y)|/|E_0|$ maps for a gap $g_x = 2$ nm above the capping layer/air interface at (a),(c) $z = 3$ nm and (b),(d) $z = 5$ nm for (a),(b) Au nanoparticles and (c),(d) Ag nanoparticles. Dotted lines indicate dimensions and position of the nanoparticle at $z = 0$ nm.

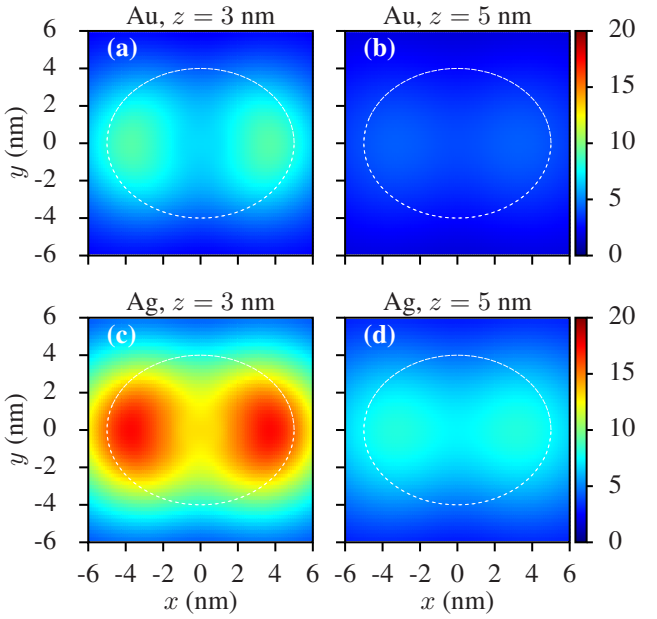


**Fig. 13** Field enhancement $|E(x, y)|/|E_0|$ maps for a gap $g_x = 14$ nm above the capping layer/air interface at (a),(c) $z = 3$ nm and (b),(d) $z = 5$ nm for (a),(b) Au nanoparticles and (c),(d) Ag nanoparticles. Dotted lines indicate dimensions and position of the nanoparticle at $z = 0$ nm.

electric field. Therefore, when the nanoparticles are covered by a capping-layer thicker than 5 nm, a smaller gap does not increase the electric field at the capping layer/air interface compared to isolated nanoparticles. In conclusion, our results provide evidence that, for SERS-type applications with protected nanoparticles, it would be preferable to use pure metal, Ag or Au, instead of $Ag_xAu_{1-x}$ nanoparticles with a capping layer as thin as possible while ensuring both chemical stability and limited atomic diffusion of the metal. Finally, the best field-enhancement effect at the capping layer/air interface results from a delicate balance, which

depends not only on the composition and morphology (size and shape) of the nanoparticles, but also on the interparticle gap, the capping-layer thickness, and the refractive index of the surrounding matrix.

**Acknowledgements** The authors are grateful to P. Guérin for assistance during the growth of $Ag_xAu_{1-x}$ thin films by ion-beam sputtering deposition. This work has been partially funded by the French National Agency (QMAX project no. ANR-09-NANO-031) in the frame of its 2009 programme in Nanosciences, Nanotechnologies and Nanosystems (P3N2009).

## References

1. U. Kreibig, M. Vollmer, *Optical properties of metal clusters* (Springer-Verlag, Berlin, Heidelberg, 1995)
2. C.F. Bohren, D.R. Huffman, *Absorption and scattering of light by small particles* (John Wiley & Sons, 1998)
3. H.A. Atwater, A. Polman, Nat. Mater. **9**(3), 205 (2010).
4. P. Anger, P. Bharadwaj, L. Novotny, Phys. Rev. Lett. **96**, 113002 (2006).
5. E. Fort, S. Grésillon, J. Phys. D: Appl. Phys. **41**(1), 013001 (2008).
6. N.G. Khlebtsov, L.A. Dykman, J. Quant. Spectrosc. Radiat. Transf. **111**(1), 1 (2010).
7. M. Fan, G.F.S. Andrade, A.G. Brolo, Anal. Chim. Acta **693**(12), 7 (2011).
8. N. Guillot, M. Lamy de la Chapelle, J. Nanophotonics **6**(1), 064506 (2012).
9. T.W.H. Oates, A. Keller, S. Facsko, A. Mücklich, Plasmonics **2**(2), 47 (2007).
10. A. Toma, D. Chiappe, D. Massabò, C. Boragno, F. Buatier de Mongeot, Appl. Phys. Lett. **93**(16), 163104 (2008).
11. F. Cuccureddu, S. Murphy, I.V. Shvets, M. Porcu, H.W. Zandbergen, Nano Letters **8**(10), 3248 (2008).
12. S. Camelio, D. Babonneau, D. Lantiat, L. Simonot, F. Pailloux, Phys. Rev. B **80**, 155434 (2009).
13. M. Ranjan, S. Facsko, Nanotechnology **23**(48), 485307 (2012).
14. R. Verre, K. Fleischer, O. Ualibek, I.V. Shvets, Appl. Phys. Lett. **100**, 031102 (2012).
15. O. Ualibek, R. Verre, B. Bulfin, V. Usov, K. Fleischer, J.F. McGilp, I.V. Shvets, Nanoscale **5**, 4923 (2013).
16. S. Camelio, E. Vandenhecke, S. Rousselet, D. Babonneau, Nanotechnology **25**(3), 035706 (2014).
17. D. Babonneau, S. Camelio, L. Simonot, F. Pailloux, P. Guérin, B. Lamongie, O. Lyon, EPL **93**(2), 26005 (2011).
18. L. Anghinolfi, R. Moroni, L. Mattera, M. Canepa, F. Bisio, J. Phys. Chem. C **115**(29), 14036 (2011).
19. A. Belardini, M.C. Larciprete, M. Centini, E. Fazio, C. Sibilia, D. Chiappe, C. Martella, A. Toma, M. Giordano, F. Buatier de Mongeot, Phys. Rev. Lett. **107**, 257401 (2011).
20. S.A. Khan, D.K. Avasthi, D.C. Agarwal, U.B. Singh, D. Kabiraj, Nanotechnology **22**(23), 235305 (2011).
21. G. Maidecchi, G. Gonella, R.P. Zaccaria, R. Moroni, L. Anghinolfi, A. Giglia, S. Nannarone, L. Mattera, H.L. Dai, M. Canepa, F. Bisio, ACS Nano **7**(7), 5834 (2013).
22. C. Gao, Y. Hu, M. Wang, M. Chi, Y. Yin, J. Am. Chem. Soc. **136**(20), 7474 (2014).
23. S. Besner, M. Meunier, J. Phys. Chem. C **114**(23), 10403 (2010)
24. N. Alissawi, V. Zaporojtchenko, T. Strunskus, I. Kocabas, V. Chakravadhanula, L. Kienle, D. Garbe-Schnberg, F. Faupel, Gold Bull. **46**(1), 3 (2013).
25. J. Sanchez-Ramirez, U. Pal, L. Nolasco-Hernandez, J. Mendoza-Alvarez, J. Pescador-Rojas, J. Nanomaterials **2008** (2008)
26. R. Kuladeep, L. Jyothi, K.S. Alee, K.L.N. Deepak, D.N. Rao, Opt. Mater. Express **2**(2), 161 (2012).
27. M.B. Cortie, A.M. McDonagh, Chem. Rev. **111**(6), 3713 (2011).
28. M. Gaudry, J. Lermé, E. Cottancin, M. Pellarin, J.L. Vialle, M. Broyer, B. Prével, M. Treilleux, P. Mélinon, Phys. Rev. B **64**, 085407 (2001).
29. W. Benten, N. Nilius, N. Ernst, H.J. Freund, Phys. Rev. B **72**, 045403 (2005).
30. F. Gonella, E. Cattaruzza, G. Battaglin, F. D'Acapito, C. Sada, P. Mazzoldi, C. Maurizio, G. Mattei, A. Martorana, A. Longo, F. Zontone, J. Non-Cryst. Solids **280**(13), 241 (2001).
31. R.K. Roy, S.K. Mandal, A.K. Pal, Eur. Phys. J. B **33**(1), 109 (2003).
32. J. Sancho-Parramon, V. Janicki, M. Lončarić, H. Zorc, P. Dubček, S. Bernstorff, Appl. Phys. A **103**(3), 745 (2011).
33. H.T. Beyene, V.S.K. Chakravadhanula, C. Hanisch, M. Elbahri, T. Strunskus, V. Zaporojtchenko, L. Kienle, F. Faupel, J. Mater. Sci. **45**(21), 5865 (2010).
34. Y. Nishijima, S. Akiyama, Opt. Mater. Express **2**(9), 1226 (2012).
35. S. Link, Z.L. Wang, M.A. El-Sayed, J. Phys. Chem. B **103**(18), 3529 (1999).
36. P. Mulvaney, Langmuir **12**(3), 788 (1996).
37. M. Brauwers, F. Brouers, Phys. Status Solidi B **75**(2), 519 (1976).
38. O. Peña-Rodríguez, M. Caro, A. Rivera, J. Olivares, J.M. Perlado, A. Caro, Opt. Mater. Express **4**(2), 403 (2014).
39. J. Rivory, Phys. Rev. B **15**, 3119 (1977).
40. H.U. Yang, J. D'Archangel, M.L. Sundheimer, E. Tucker, G.D. Boreman, M.B. Raschke, Phys. Rev. B **91**, 235137 (2015).
41. Y. Jiang, S. Pillai, M.A. Green, Opt. Express **23**(3), 2133 (2015).
42. S. Yazidi, A. Fafin, S. Rousselet, F. Pailloux, S. Camelio, D. Babonneau, Phys. Status Solidi C pp. n/a–n/a (2015).
43. P.B. Johnson, R.W. Christy, Phys. Rev. B **6**, 4370 (1972).
44. J.C. Tinguely, I. Sow, C. Leiner, J. Grand, A. Hohenau, N. Felidj, J. Aubard, J. Krenn, BioNanoScience **1**(4), 128 (2011).
45. D. Rioux, S. Vallières, S. Besner, P. Muñoz, E. Mazur, M. Meunier, Adv. Opt. Mater. **2**(2), 176 (2014).
46. J. Banhart, Phys. Rev. Lett. **82**, 2139 (1999).
47. R. Rajendra, P. Bhatia, A. Justin, S. Sharma, N. Ballav, J. Phys. Chem. C **119**(10), 5604 (2015).
48. *Lumerical Solutions, Inc.* http://www.lumerical.com/tcad-products/fdtd/
49. V. Myroshnychenko, J. Rodriguez-Fernandez, I. Pastoriza-Santos, A.M. Funston, C. Novo, P. Mulvaney, L.M. Liz-Marzan, F.J. Garcia de Abajo, Chem. Soc. Rev. **37**, 1792 (2008).
50. J.P. Berenger, J. Comput. Phys. **114**(2), 185 (1994).
51. B. Rodriguez-Gonzalez, A. Sanchez-Iglesias, M. Giersig, L.M. Liz-Marzan, Farad. Discuss. **125**, 133 (2004).
52. S.W. Verbruggen, M. Keulemans, J.A. Martens, S. Lenaerts, J. Phys. Chem. C **117**(37), 19142 (2013).
53. P.K. Jain, W. Huang, M.A. El-Sayed, Nano Lett. **7**(7), 2080 (2007).

54. P.K. Jain, M.A. El-Sayed, J. Phys. Chem. C **112**(13), 4954 (2008).
55. C. Tabor, D. Van Haute, M.A. El-Sayed, ACS Nano **3**(11), 3670 (2009).
56. E. Hao, G. Schatz, J. Chem. Phys. **120**(1), 357 (2004).